Ground-state phase diagram and parity-flipping microwave transitions in a gate-tunable Josephson junction

M. R. Sahu,[1,*] F. J. Matute-Cañadas,[2,*] M. Benito,[1] P. Krogstrup,[3,4] J. Nygård,[4] M. F. Goffman,[1] C. Urbina,[1] A. Levy Yeyati,[2] and H. Pothier[1,†]

[1]*Quantronics group, Service de Physique de l'État Condensé (CNRS, UMR 3680), IRAMIS, CEA-Saclay, Université Paris-Saclay, 91191 Gif-sur-Yvette, France*

[2]*Departamento de Física Teórica de la Materia Condensada, Condensed Matter Physics Center (IFIMAC) and Instituto Nicolás Cabrera, Universidad Autónoma de Madrid, 28049 Madrid, Spain*

[3]*NNF Quantum Computing Programme, Niels Bohr Institute, University of Copenhagen, Universitetsparken 5, 2100 Copenhagen, Denmark*

[4]*Center for Quantum Devices, Niels Bohr Institute, University of Copenhagen, Universitetsparken 5, 2100 Copenhagen, Denmark*

(Received 20 December 2023; accepted 19 March 2024; published 5 April 2024)

We probed a gate-tunable InAs nanowire Josephson weak link by coupling it to a microwave resonator. Tracking the resonator frequency shift when the weak link is close to pinch-off, we observe that the ground state of the latter alternates between a singlet and a doublet when varying either the gate voltage or the superconducting phase difference across it. The corresponding microwave absorption spectra display lines that approach zero energy close to the singlet-doublet boundaries, suggesting parity-flipping transitions, which are in principle forbidden in microwave spectroscopy and expected to arise only in tunnel spectroscopy. We tentatively interpret them by means of an ancillary state isolated in the junction acting as a reservoir for individual electrons.

DOI: 10.1103/PhysRevB.109.134506

I. INTRODUCTION

Particle number parity effects are widespread in mesoscopic superconductivity [1,2]. They appeared in circuits containing small metallic superconducting islands [3–7] and in semiconductor-superconductor hybrids, like a quantum dot coupled to superconducting electrodes through tunnel barriers [8]. In these systems, the electrodynamics depends crucially on charging effects in the island or the quantum dot [9]. More recently, parity effects were shown to arise in mesoscopic Josephson weak links, structures containing no island or quantum dots and therefore no significant charging energy. Here, the physics is understood in terms of a few Andreev bound states (ABSs), subgap localized quasiparticle states with energies governed by the superconducting phase difference across the weak link. The odd or even many-body occupations of these states result in markedly different weak link electrodynamic properties. They are probed using microwave circuit-QED (cQED) techniques, microwave absorption spectroscopy, quasiparticle addition spectroscopy, and combinations of them [10–13]. In the case of infinitely short weak links, realized with atomic contacts between two superconducting leads [14], all the observed features are explained in terms of noninteracting junction models [15]. There is also a wealth of experimental results on gate-tunable, finite-length weak links, based on semiconducting nanowires and which are also described in terms of ABSs [16–21]. There is recent evidence that in these weak links, even with well-transmitted conduction channels, interactions play a role, albeit just as a small perturbation [22,23]. When approaching pinch-off in the same devices, one expects quantum-dot physics to become relevant and influence the parity dynamics.

Here, we present cQED measurements on gate-tunable InAs nanowire weak links [24] close to pinch-off. We observe, both as a function of gate voltage and phase difference, features that we associate with transitions between ground states of different parity, like what is observed in quantum dots. Remarkably, the corresponding microwave absorption spectra exhibit transition lines that, as a function of gate voltage, bear a close resemblance with those typically observed in an addition spectrum [12,25] and therefore seem to couple states of different parities, a forbidden process in photon absorption spectroscopy. We interpret these results as revealing the presence of an ancillary, weakly coupled quantum level, which allows mimicking parity transitions on the main transport channel without a change in the global parity.

II. BASIC CONCEPTS

When a few-channel conductor connects two superconductors in a phase-biased configuration, various regimes are encountered depending on the relative size of the coupling to the leads Γ, the Coulomb repulsive energy U, and the superconducting gap Δ [2,26]. In the limit of large coupling, the system is well described by electrons and holes bouncing back and forth between the electrodes, with Andreev reflections at each interface, giving rise to supercurrent-carrying ABSs [27–29]. The opposite limit is that of a quantum dot weakly coupled to the superconducting leads, usually described using a single-level Anderson impurity model [26,30–39], as

*These authors contributed equally to this work.
†Corresponding author: hugues.pothier@cea.fr

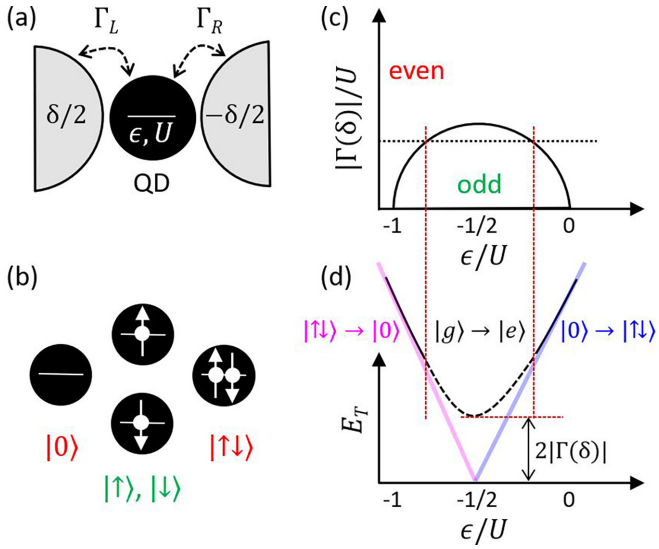

FIG. 1. (a) Scheme of the superconducting single-level Anderson model. (b) The four states correspond to the possible occupancies of the quantum-dot level. (c) Phase diagram for model in the infinite gap limit. (d) Black curve represents the energy E_T of the transition $|g\rangle \rightarrow |e\rangle$, with $|g\rangle$ and $|e\rangle$ the ground and excited states in the even parity sector, for a given $\Gamma(\delta)$ represented as a horizontal dotted line in (c). The dashed part of the curve should not be visible in the zero temperature limit, as it corresponds to the odd ground-state region. States $|g\rangle$ and $|e\rangle$ are linear combinations of the dot states $|0\rangle$ and $|\uparrow\downarrow\rangle$, hybridized by the effective pairing $\Gamma(\delta)$. Blue and magenta straight lines correspond to the limiting cases when $\Gamma(\delta) = 0$.

schematically presented in Fig. 1(a). The energy ϵ of the dot level (referred to the Fermi level of the leads) can be tuned by means of an electrostatic gate. In the absence of a magnetic field, the level is spin-degenerate, and the four possible dot states $|0\rangle$, $|\uparrow\rangle$, $|\downarrow\rangle$, and $|\uparrow\downarrow\rangle$ shown in Fig. 1(b), characterized by the level occupation, split into two categories. When the dot occupancy is even (states $|0\rangle$ or $|\uparrow\downarrow\rangle$), the corresponding energies are 0 and $2\epsilon + U$. When the occupancy is odd, the spin-degenerate state $|\sigma\rangle$ has energy ϵ. One finds that the ground state of the dot is odd if $-1 < \epsilon/U < 0$, and it is even otherwise [see Fig. 1(c)]. Increasing the coupling to the superconducting leads favors a singlet superposition of the even states $|g\rangle$, while gradually diminishing the extension of the odd (doublet) ground state in the phase diagram. This effect is most simply captured in the infinite gap limit, where the effective pairing is given by $\Gamma(\delta) = \Gamma_L e^{i\delta/2} + \Gamma_R e^{-i\delta/2}$, with $\Gamma_{L,R}$ the tunneling rates to the left and right leads and δ the superconducting phase difference between the two leads [26,40]. This behavior has been investigated in a number of works [12,16,25,41–44] and revived by recent experiments using microwave techniques [23,45,46]. Finally, Fig. 1(d) shows the ϵ dependence of the transition energy from the even ground state $|g\rangle$ toward the even excited state $|e\rangle$.

III. EXPERIMENTAL RESULTS

The experimental setup is schematized in Fig. 2(a). An InAs nanowire weak link is placed in a superconducting loop threaded by a magnetic flux Φ. The phase difference δ across the weak link is given by $\delta = 2\pi\Phi/\Phi_0$, with $\Phi_0 = h/2e$ the flux quantum. The wire is suspended over a metallic

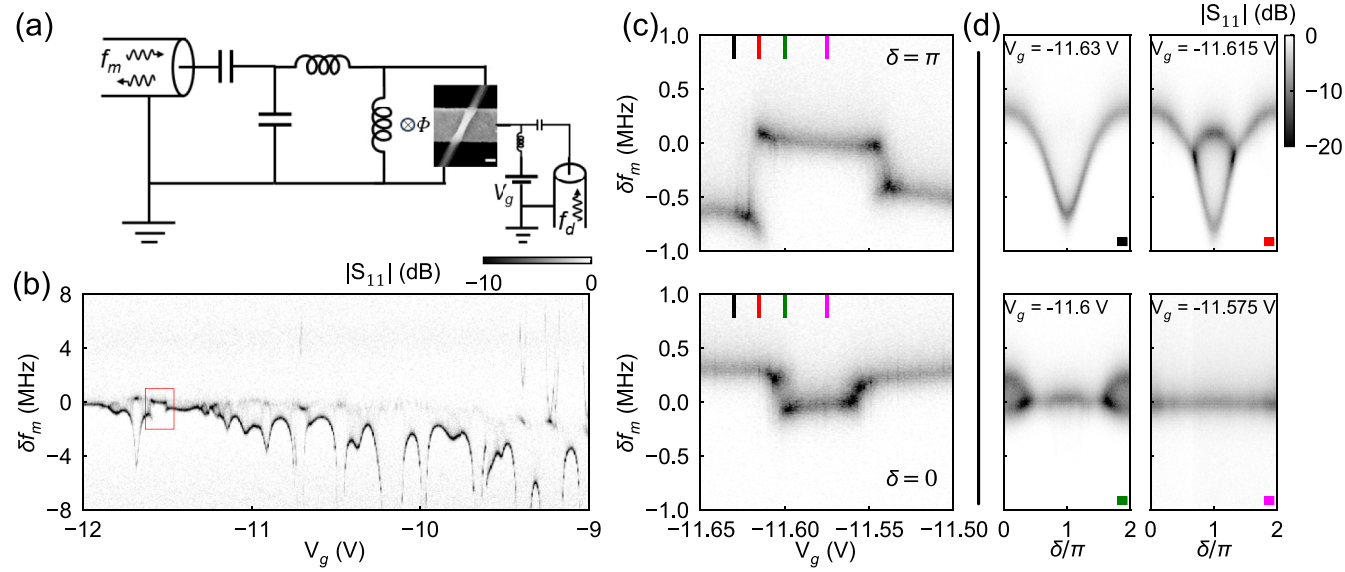

FIG. 2. (a) Schematic of the measurement setup with scanning electron microscopy (SEM) image (scale bar, 200 nm) of the InAs nanowire weak link. f_m is the measurement frequency, V_g the gate voltage, and f_d the drive frequency applied to the gate electrode through a bias tee in two-tone spectroscopy measurements. Φ is the magnetic flux related to phase difference δ by $\delta = 2\pi\Phi/\Phi_0$, with $\Phi_0 = h/2e$ the flux quantum. (b) 2D grayscale map of the amplitude of reflection coefficient $|S_{11}|$ plotted as a function of $\delta f_m = f_m - f_0$ and V_g, at phase difference $\delta = \pi$. (c) Upper panel: A higher-resolution 2D grayscale map of the single-tone spectrum $|S_{11}|(V_g, \delta f_m)$ at $\delta = \pi$ in the highlighted region of (b). Lower panel: Corresponding 2D map of $|S_{11}|(V_g, \delta f_m)$ at $\delta = 0$. (d) 2D grayscale map of $|S_{11}|$ plotted as a function of δf_m [as in (b) and (c)] and phase difference (δ/π) at several gate voltages ($V_g = -11.63, -11.615, -11.6$, and -11.575 V) marked by vertical ticks in (c) sharing the same color as the squares at the bottom right of the corresponding panels in (d).

gate, biased at voltage V_g, which allows us to control the electron density. The loop participates in the inductance of a quarter-wavelength coplanar wave-guide resonator made out of NbTiN. The occupation of the Andreev states in the nanowire is inferred from the (complex) reflection coefficient of a microwave tone at frequency f_m close to the bare resonance frequency $f_0 = 7.00\,\mathrm{GHz}$ of the resonator measured when the weak link is fully depleted. The total quality factor of the resonator is $Q = 23\,000$. A second tone (drive tone) with frequency f_d, applied through the gate line, allows probing the absorption excitation spectrum of the weak link. A detailed discussion of measurement setup and device fabrication is presented in Supplemental Material (SM) [47].

First, we present the single-tone measurements of the reflection coefficient S_{11}. The amplitude $|S_{11}(\delta f_m)|$, where $\delta f_m = f_m - f_0$, is presented as a function of V_g in Fig. 2(b). Dark lines mark minima of $|S_{11}|$ associated with the resonance frequency of the resonator modified by the occupation of Andreev states in the weak link. Highly dispersing lines can be related to pair transitions with gate-modulated transition energies [38,39,48,49]. When V_g approaches $-12\,\mathrm{V}$, the oscillations of the resonance frequency fade away, marking the complete depletion of the nanowire. All along the scan, one also observes a weak resonance at $\delta f_m \approx 0$, which corresponds to a state very weakly coupled to the resonator [48].

Unique jumps in the resonance frequency are observed close to pinch-off in the single-tone data in Fig. 2(b). One such region is highlighted by a red rectangle around $V_g = -11.6$ V. A higher-resolution measurement of single-tone spectra around this highlighted region at $\delta = \pi$ is shown in the upper panel of Fig. 2(c). Similar jumps are observed for $\delta = 0$, as shown in the lower panel of Fig. 2(c). The central plateaus in both plots correspond to resonance frequencies very close to the bare resonance frequency f_0, whereas the outer regions appear at $f_m < f_0$ for $\delta = \pi$ and at $f_m > f_0$ for $\delta = 0$. To better understand these behaviors, two-dimensional (2D) grayscale maps of $|S_{11}|$ as a function of phase difference δ and frequency δf_m are plotted in Fig. 2(d), at several gate voltages. At $V_g = -11.63$ V (top left), we observe a single transition frequency strongly dispersing with phase, which is expected for the supercurrent-carrying even (singlet) ground state in the single-level Anderson model. In contrast, at $V_g = -11.575$ V (bottom right), the resonance frequency is almost phase independent and lies very close to $\delta f_m = 0$, close to behavior of an odd (doublet) ground state with suppressed supercurrent. From these observations, we infer that a strong signal on the central plateau of the resonances in Fig. 2(c) corresponds to an oddlike ground state and that a strong signal on the outer regions corresponds to an evenlike ground state. As can be seen from the top-right and bottom-left panels of Fig. 2(d), at intermediate gate voltages, we observe either one or two resonance frequencies depending on phase, which indicate a phase diagram of the singlet/doublet ground states that not only depends on V_g but also on the phase difference δ [23,45].

The single-tone results shown in Fig. 2 are measurements of S_{11} averaged over a long (33 μs) duration at a given f_m. It reflects the different values, corresponding to different ABS occupations, taken by S_{11} during the averaging time. Information about the ABS occupation dynamics can be accessed by performing a series of successive short measurements of S_{11}. We performed 50 000 measurements of S_{11} at a frequency close to f_0, with a time per point of 500 ns, each measurement producing a mean value of real (in-phase, I) and imaginary (quadrature, Q) components. Using these 50 000 I and Q data, we plot histograms in the IQ plane, as shown in Fig. 3(a), at three settings of V_g around one of the regions where we observe the jump in resonance frequency in Fig. 2(c). We observe two clouds in the IQ plane, which correspond to the lower-energy even and odd states of the weak link. By using a Gaussian mixture model (GMM) [50], we extracted the population of the two states (P_o and P_e correspond to populations of the oddlike and evenlike states, respectively) as a function of V_g at $\delta = \pi$ [Fig. 3(b)] and at $\delta = 0$ [Fig. 3(d)]. The V_g region for which the oddlike state is observed is larger at $\delta = \pi$ than at $\delta = 0$. In Fig. 3(c), we show the 2D color map of polarization $P_o - P_e$ as a function of V_g and δ, showing the full phase diagram of the singlet-doublet phase transition. In the region around $\delta/\pi \sim 0.5$, the clouds overlap, and GMM prediction does not work. The procedure also fails when only one state is visible (strong polarization).

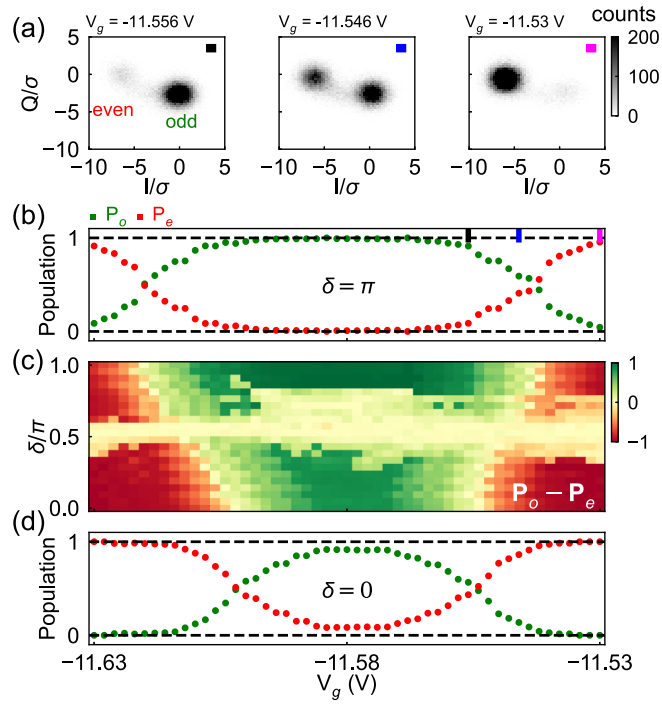

FIG. 3. (a) Histogram of 50 000 measurements of S_{11} at a fixed measurement frequency close to f_0 in the IQ plane, at gate voltages $V_g = -11.556$, -11.546, and -11.53 V, respectively. Each measurement produces mean I and mean Q over a 500 ns measurement duration. (b) Population of oddlike state P_o (green) and evenlike state P_e (red) are plotted as a function of V_g at $\delta = \pi$. (c) 2D color map of polarization $P_o - P_e$ plotted as a function of V_g and δ/π. (d) P_o and P_e plotted as a function of V_g at $\delta = 0$.

Lifetimes of the singlet and doublet states can be evaluated by performing a continuous version of the above measurement, which is presented in detail in the SM [47]. When the population of one of the states is ∼1, we observed its lifetime to be of the order of a millisecond with the lifetime

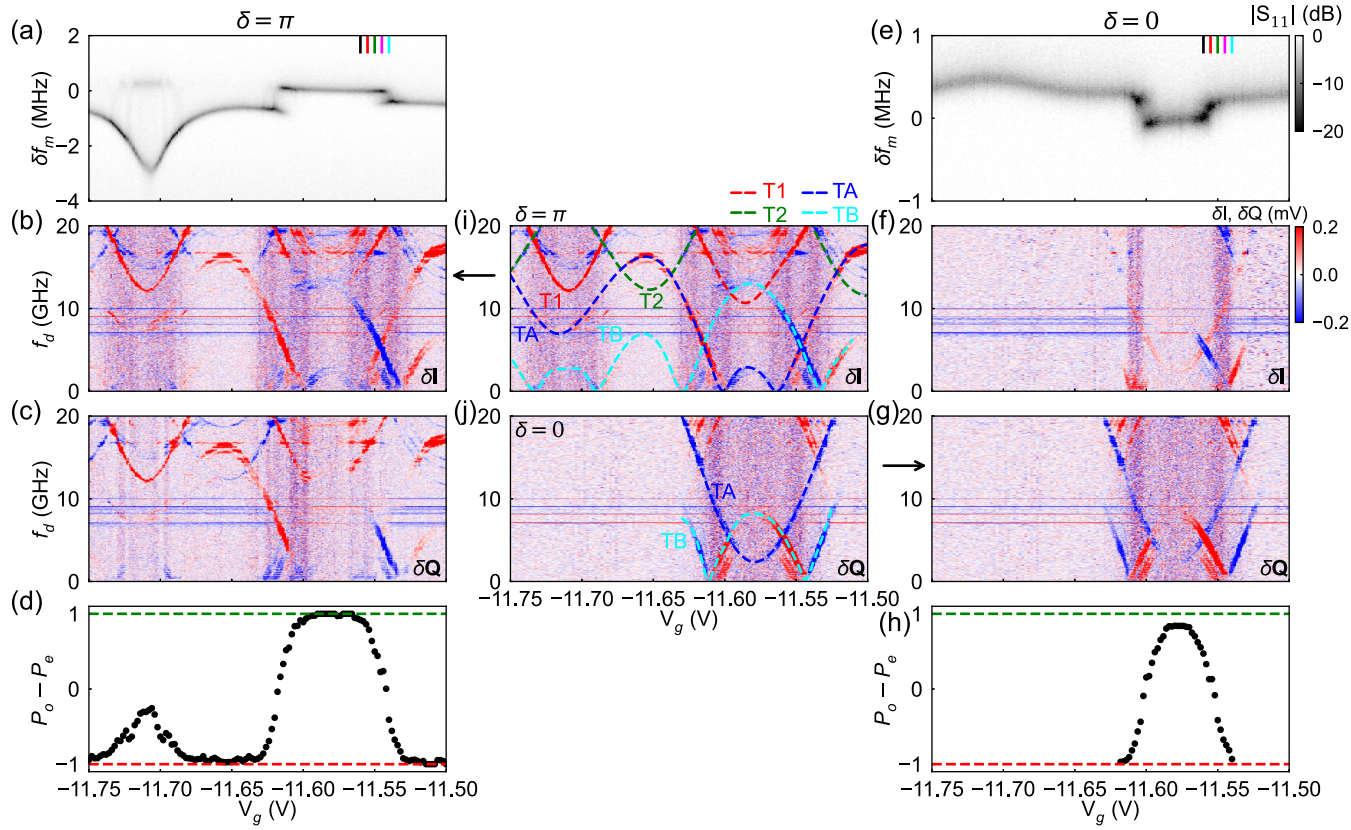

FIG. 4. (a) 2D grayscale map of single-tone spectrum $|S_{11}|(V_g, \delta f_m)$ at $\delta = \pi$. (b) and (c) 2D color map of δI and δQ components of the two-tone spectroscopy, respectively, plotted as a function of drive frequency f_d and V_g, at $\delta = \pi$. (d) Polarization $P_o - P_e$ plotted as a function of V_g. Polarization $= -1$ (red dashed line) implies fully evenlike ground state, polarization $= 1$ (green dashed line) implies fully oddlike ground state. (e)–(h) Same as (a)–(d) at $\delta = 0$. (i) Duplicate of (b), where the four transitions T1 (red), T2 (green), TA (blue), and TB (cyan) are highlighted by dashed lines at $\delta = \pi$. (j) Duplicate of (g), where the TA (blue) and TB (cyan) are highlighted by dashed lines at $\delta = 0$.

of the other state being a few microseconds, like an earlier experiment [45].

The observations from Figs. 2 and 3 can be qualitatively understood by the fact that, close to the pinch-off, the coupling of the weak link to the superconducting leads can be significantly reduced, so that it behaves like a quantum dot. The system can then be modeled by a single-level Anderson model, which in the infinite gap limit produces the phase diagram of singlet-doublet ground states shown in Fig. 1(c) [39,40]. In our experiment, the gate voltage mainly tunes the position of the energy level, whereas the phase difference between the superconducting leads tunes the effective coupling $\Gamma(\delta) = \Gamma_L e^{i\delta/2} + \Gamma_R e^{-i\delta/2}$. The fact that $\Gamma_\pi = \Gamma_L - \Gamma_R$ is lower in magnitude than $\Gamma_0 = \Gamma_L + \Gamma_R$ explains why the doublet is observed over a larger range of V_g at $\delta = \pi$ than at $\delta = 0$.

We now present the two-tone spectroscopy results, which are measurements of the change in the reflection coefficient S_{11} at a fixed frequency f_m in the presence of a drive tone with variable frequency f_d. For a given f_d, the I and Q components of S_{11} are measured both when the drive is on and off, and the differences δI and δQ are recorded. In Figs. 4(b) and 4(c), we show the 2D color map of δI and δQ as a function of V_g and f_d, at phase difference $\delta = \pi$. We use the 2D color map of δI in Fig. 4(i) to highlight with dashed curves the four transitions that we will be discussing in the following. Transitions T1 and T2 (red and green) have rounded minima at finite frequency. This behavior is generic in Andreev nanowire weak links [19,51]. In contrast, transitions TA and TB, which reach zero frequency (within experimental accuracy) with cusps, are anomalous, and we observe them only near pinch-off. They resemble tunneling spectroscopy data in superconducting quantum dots, where they are associated with a quantum phase transition between even and odd ground states [12]. In addition, TA and TB correspond to population transfer between the even and odd clouds shown in Fig. 3(a) (more details in the SM [47]). As will be discussed in Sec. III, we could reproduce them by introducing an ancillary level to the single-level Anderson model. In Figs. 4(a) and 4(d), we plot the single-tone spectrum and polarization $P_o - P_e$, respectively, as a function of V_g at $\delta = \pi$. Interestingly, TA and TB intersect at the gate voltages very close to the singlet-to-doublet phase transition points, i.e., around the gate voltages where the polarization changes sign.

When changing the phase from π to 0, line TB changes but still exhibits cusps at zero frequency, while TA shifts up and does not reach zero frequency any longer, as shown in Figs. 4(e)–4(h) and 4(j).

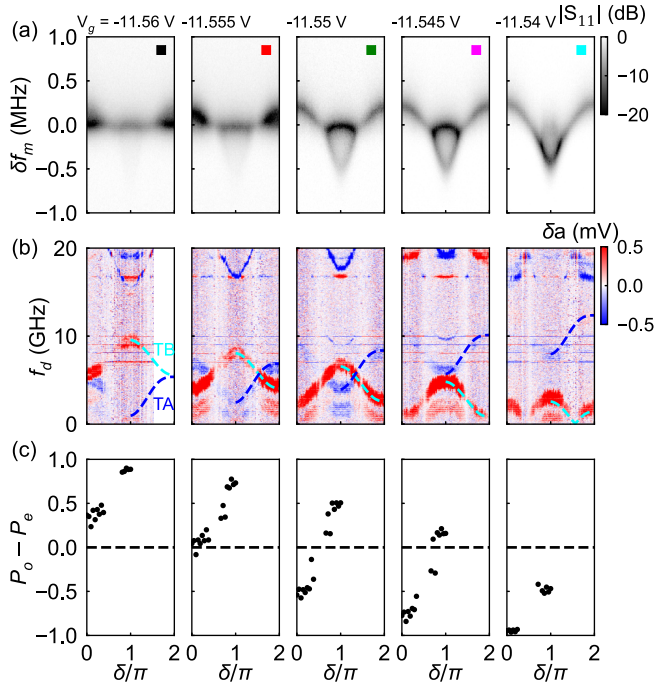

FIG. 5. (a) 2D grayscale map of single-tone spectrum $|S_{11}|(\delta, \delta f_m)$ at gate voltages $V_g = -11.56$, -11.555, -11.55, -11.545, and -11.54 V, respectively [marked as colored vertical lines in Figs. 3(b) and 3(c)]. (b) 2D color maps of two-tone spectrum $\delta a(\delta, f_d)$. (c) Polarization $P_o - P_e$ as a function of δ, measured between 0 and π. Missing data at certain values of δ correspond to situations where the Gaussian mixture model (GMM) prediction does not work.

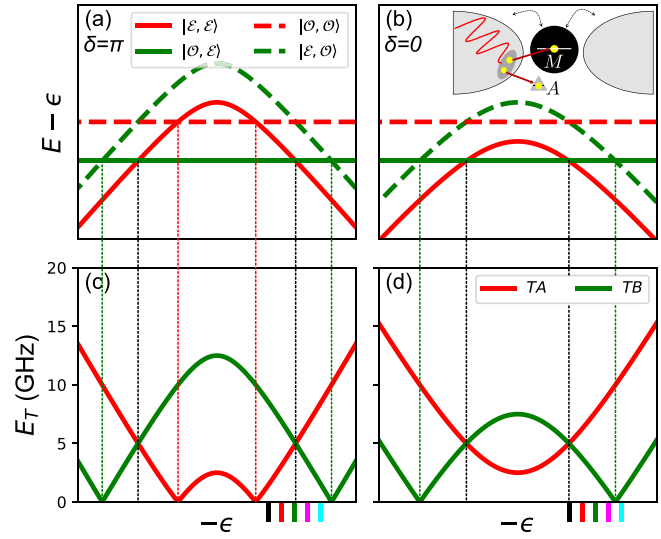

FIG. 6. Upper row: Lowest many-body energies of the ancillary level model over the position ϵ of the main channel level, at phase differences (a) $\delta = \pi$ and (b) 0. Energies are plotted with a global shift of ϵ and indicate even (odd) global parity with red (green) color, and empty (filled) occupation in the ancillary level with solid (dashed) lines (second entry of ket $|M, A\rangle$). Inset in (b) represents the mechanism of local parity flip. Lower row: Corresponding global parity-conserving transitions. Vertical dotted lines are placed at the singlet/doublet boundaries in the main channel (black) and at the crossings between states with the same global parity (red/green). Parameters are chosen to qualitatively reproduce the two-tone measurements in Fig. 4 around the gate range $V_g \in [-11.65, -11.50]$ V (see SM [47]): $\Gamma_L = 2.5$, $\Gamma_R = 8$, $\epsilon_A = 5$, and $U = 26$ (units in GHz).

Now we present the phase dependence of the two-tone spectra at several gate voltages in Fig. 5(b), together with the corresponding single-tone measurements in Fig. 5(a) and polarization in Fig. 5(c). The color code of the 2D color maps in Fig. 5(b) represents the amplitude (δa) of the shift of S_{11} in a δ-dependent phase direction in the IQ plane, such that the contrast of TA is maximized (more details in the SM [47]). In the right half of each panel of Fig. 5(b), the TA and TB are highlighted with dashed lines with same colors as Figs. 4(b) and 4(f), i.e., blue and cyan, respectively. For the five gate voltages shown in Fig. 5, the single-tone data in Fig. 5(a) as well as the corresponding population data in Fig. 5(c) show the gradual shrinking of the region for which the oddlike ground state is observed. The spacing between the crossing points of TA and TB also follows a similar decreasing trend. These observations are consistent with the theoretical model discussed below.

IV. ANCILLARY-LEVEL MODEL

We now focus on the two lowest transition lines (TA and TB) vs gate voltage in the range where they exhibit cusps with cusps close to zero drive frequency (Fig. 4). A possible explanation for these cusps is the occurrence of replicas involving the absorption or emission of a resonator photon with energy hf_r, thus appearing at energies $E_T \pm hf_r$, where E_T is the bare transition energy. In the case where $E_T < hf_r$ and there is a significant population in the excited weak link state, there would also appear transition lines with energy $-E_T + hf_r$ corresponding to the excitation of a resonator photon with relaxation in the weak link. This set of replica lines gives rise to cusps when E_T crosses hf_r. However, in our case, the replica mechanism should be discarded for the following reasons. On the one hand, if one of these anomalous transitions were a replica of the other one (as their constant vertical separation $\sim$11 GHz in frequency suggests), one would still need to explain the appearance of cusps in the other anomalous line. Moreover, the constant shift $\sim$11 GHz should correspond to one spurious resonator mode, which is not visible in the spectra. On the other hand, the anomalous lines cannot be replicas of transition lines T1 and T2, as illustrated in Fig. S9 in the SM [47]. Ultimately, the highly symmetric disposition of the cusps and their proximity with the singlet-doublet boundaries hint at a different mechanism.

Indeed, when just one line is considered, its cusps close to the singlet-doublet boundaries suggest that it connects the singlet with the doublet states, as their energy difference crosses zero at the boundaries. Connecting singlet to doublet states when exciting with microwaves is forbidden because parity should be conserved. However, the situation changes if an ancillary dot level A, weakly coupled to the main channel M, is added to the model [see inset in Fig. 6(b)]. This configuration

allows us to explain the other line as well and has already been used to describe some transport experiments in semiconducting nanowire Josephson junctions [52]. We model it with a Hamiltonian $H = H_M + H_A$ such that

$$H_M = \sum_\sigma \epsilon d_\sigma^\dagger d_\sigma + U n_\uparrow n_\downarrow + (\Gamma(\delta) d_\uparrow^\dagger d_\downarrow^\dagger + \text{H.c.}), \quad (1)$$

where $d_\sigma^\dagger$ creates an electron with spin σ on the dot and $n_\sigma = d_\sigma^\dagger d_\sigma$, corresponds to the infinite gap Anderson model described above; and

$$H_A = \sum_\sigma \epsilon_A d_{A\sigma}^\dagger d_{A\sigma} + U_A n_{A\uparrow} n_{A\downarrow} + (t_A d_{A\sigma}^\dagger d_\sigma + \text{H.c.}) \quad (2)$$

describes the ancillary dot level ϵ_A, weakly coupled to the main channel by a vanishing tunnel amplitude t_A and endowed with a charging energy U_A that forbids its double occupation.

When restricted to the main channel, the lowest-energy levels in each parity sector even ($\mathcal{E}$) and odd ($\mathcal{O}$) are

$$|\mathcal{E}\rangle_M = u\,|0\rangle_M - v e^{i\theta}\,|\uparrow\downarrow\rangle_M \to E_\mathcal{E} = \xi - \sqrt{\xi^2 + |\Gamma(\delta)|^2},$$
$$|\mathcal{O}\rangle_M = |\sigma\rangle_M \to E_\mathcal{O} = \epsilon, \quad (3)$$

with $\xi = \epsilon + U/2$, $u(v) = \frac{1}{\sqrt{2}}\sqrt{1 \pm \xi/\sqrt{\xi^2 + |\Gamma(\delta)|^2}}$ and $e^{i\theta} = \Gamma(\delta)/|\Gamma(\delta)|$. The corresponding energies as a function of ϵ are shown with red (even) and green (odd) solid lines in Fig. 6(a) ($\delta = 0$) and Fig. 6(b) ($\delta = \pi$), whose crossings indicate a parity switch of the ground state (vertical black dotted lines).

When the ancillary state is introduced ($|\mathcal{E}\rangle_A = |0\rangle_A$, $|\mathcal{O}\rangle_A = |\sigma\rangle_A$), for vanishing t_A, the many-body energy levels of the whole system $|M, A\rangle$ are

$$|\mathcal{E},\mathcal{E}\rangle \to E_\mathcal{E}, \quad |\mathcal{E},\mathcal{O}\rangle \to E_\mathcal{E} + \epsilon_A,$$
$$|\mathcal{O},\mathcal{E}\rangle \to E_\mathcal{O}, \quad |\mathcal{O},\mathcal{O}\rangle \to E_\mathcal{O} + \epsilon_A, \quad (4)$$

which coincide with those in the main channel if the ancillary level is empty and are shifted by ϵ_A if it is occupied (we consider that the gate voltage in the analyzed range only tunes the main chain level ϵ and barely affects ϵ_A). These states with the occupied ancillary level switch the global parity with respect to the parity in the main channel and are indicated with dashed lines in Figs. 6(a) and 6(b). It should be noted that the vanishing coupling of the ancillary level to the superconducting leads renders the resonator quite insensitive to its occupation; thus, the single-tone measurements mainly probe the population in the main channel.

The corresponding global parity-conserving transitions of the whole system are shown in Figs. 6(c) and 6(d). As in the two-tone measurements in Fig. 4, they are shifted (or reflected over $E = 0$) by a constant, which in the model is $2\epsilon_A$. In addition, they intersect close to the singlet-doublet boundary of the main channel, and they may exhibit sharp cusps at its sides, depending on the number of crossings between states with the same global parity (vertical red/green dotted lines). To observe these transitions, a finite population in the lowest-energy states of both global parity sectors is needed, and this requires a finite poisoning in the main channel or in the ancillary level depending on the position of the gate.

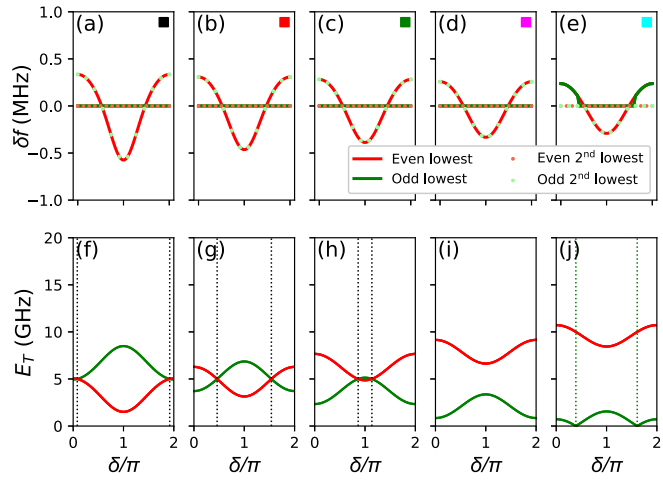

FIG. 7. (a)–(e) Frequency shift over the phase difference for a set of values of the main channel level ϵ's, corresponding to the colored markers in Fig. 6, following qualitatively those from Figs. 4 and 5. (f)–(j) Associated lowest global parity-conserving transitions. Parameters and vertical lines as in Fig. 6, and the coupling with resonator is set to $\lambda = 0.015$.

The phase dependence of the transitions for several values of the main channel level, denoted with color markers in Fig. 6, is shown in Figs. 7(f)–7(j). These results demonstrate that the model can account for the evolution of the experimental transition lines in Fig. 5(b). First, in Fig. 7(f), ϵ is placed at the singlet-doublet boundary at $\delta = 0$ [see black marker in Fig. 6(d)] and to the right of the dip in the global even sector at $\delta = \pi$ [black marker in Fig. 6(c)]. Next, the level position is raised up until the singlet-doublet boundary at $\delta = \pi$ is almost reached in Fig. 7(h) [green marker in Fig. 6(c)]. Finally, the dip in the global odd sector at $\delta = 0$ occurs for ϵ values between those in Figs. 7(i) and 7(j), the latter being placed a bit to the left of the odd dip at $\delta = \pi$.

The corresponding resonator shift δf for the two lowest levels in each parity sector is shown in Figs. 7(a)–7(e). As discussed above, in the $t_A \to 0$ limit, the shift induced by each state only depends on the main channel, so it disperses with the phase when $|M\rangle = |\mathcal{E}\rangle$ and is completely suppressed when $|M\rangle = |\mathcal{O}\rangle$. To account for the slight phase dependence of the shift in the oddlike states, it is necessary to go beyond this $\Delta \to \infty$ model, as discussed in the SM [47].

In the single-tone spectroscopy, the signal manifests the shifts induced by the states that are significantly populated over the measuring time. Though in general it is expected that most of the population dwells in the ground state, the actual steady state of the junction is determined by processes involving the quasiparticles above the gap and the coupling with the environment [53,54], which induce a nonthermal distribution.

V. CONCLUSIONS

We explored the single-tone and two-tone microwave spectroscopy in a superconducting InAs weak link close to pinch-off. Observation of jumps in the resonance frequency from the single-tone spectroscopy is understood as singlet-doublet

phase transitions that occur due to the reduction of the coupling of the weak link to the superconducting leads. We observed anomalous microwave driven transitions in two-tone spectroscopy, which mimic parity-flipping behavior. These parity-flip-mimicking transitions were tentatively understood as appearing due to the presence of an ancillary level weakly coupled to the weak link. This behavior might not be generic: We observed it in a single device, and it might depend on the particularities of a single device (geometry, defects). However, this shows how the measurement of the excitation spectrum brings crucial information about the system that is not accessible in the ground-state properties. This could be relevant for applications of hybrid structures that require a precise quantum-dot configuration, such as Andreev spin qubits implemented in quantum-dot Josephson junctions [55]. Finally, the parity-flipping transitions provide a mechanism to dynamically influence the parity population through the drive, different from the one that involves the continuum of quasiparticles above the gap [13,53,54].

ACKNOWLEDGMENTS

Technical support from P. Sénat is gratefully acknowledged. We thank P. Orfila and S. Delprat for nanofabrication support, L. Tosi for assistance in data analysis and discussions, C. Metzger, our colleagues from the Quantronics group, and G. O. Steffensen for useful discussions. We thank W. Oliver and L. Laboratories for providing us with the TWPA used in the experiment. The nanowire materials development was supported by the European Research Council under Grant Agreement No. 716655 (HEMs-DAM). M.R.S. benefited from an Investissements d'Avenir grant from Labex PALM (Grant No. ANR-10-LABX-0039-PALM). A.L.Y. and F.J.M.-C. acknowledge support from the Spanish AEI through Grant No. PID2020-117671GB-I00, through the "María de Maeztu" Programme for Units of Excellence in R&D (Grant No. MDM-2014-0377) and from Spanish Ministry of Universities (Grant No. FPU20/01871). Support by EU through Grant No. 828948 (AndQC) is also acknowledged.

[1] D. V. Averin and Y. V. Nazarov, Single-electron charging of a superconducting island, Phys. Rev. Lett. **69**, 1993 (1992).

[2] Y. V. Nazarov and Y. M. Blanter, *Quantum Transport: Introduction to Nanoscience* (Cambridge University Press, Cambridge, 2009).

[3] M. T. Tuominen, J. M. Hergenrother, T. S. Tighe, and M. Tinkham, Experimental evidence for parity-based 2*e* periodicity in a superconducting single-electron tunneling transistor, Phys. Rev. Lett. **69**, 1997 (1992).

[4] P. Lafarge, P. Joyez, D. Esteve, C. Urbina, and M. H. Devoret, Measurement of the even-odd free-energy difference of an isolated superconductor, Phys. Rev. Lett. **70**, 994 (1993).

[5] P. Lafarge, P. Joyez, D. Esteve, C. Urbina, and M. H. Devoret, Two-electron quantization of the charge on a superconductor, Nature (London) **365**, 422 (1993).

[6] P. Joyez, P. Lafarge, A. Filipe, D. Esteve, and M. H. Devoret, Observation of parity-induced suppression of Josephson tunneling in the superconducting single electron transistor, Phys. Rev. Lett. **72**, 2458 (1994).

[7] D. C. Ralph, C. T. Black, and M. Tinkham, Spectroscopic measurements of discrete electronic states in single metal particles, Phys. Rev. Lett. **74**, 3241 (1995).

[8] S. De Franceschi, L. Kouwenhoven, C. Schönenberger, and W. Wernsdorfer, Hybrid superconductor–quantum dot devices, Nat. Nanotechnol. **5**, 703 (2010).

[9] G.-L. Ingold and Y. V. Nazarov, Charge tunneling rates in ultrasmall junctions, in *Single Charge Tunneling*, edited by H. Grabert and M. H. Devoret. NATO ASI Series, Vol. 294 (Springer, Boston, 1992), pp. 21–107.

[10] C. Janvier, L. Tosi, L. Bretheau, Ç. Ö. Girit, M. Stern, P. Bertet, P. Joyez, D. Vion, D. Esteve, M. Goffman *et al.*, Coherent manipulation of Andreev states in superconducting atomic contacts, Science **349**, 1199 (2015).

[11] L. Bretheau, Ç. Ö. Girit, H. Pothier, D. Esteve, and C. Urbina, Exciting Andreev pairs in a superconducting atomic contact, Nature (London) **499**, 312 (2013).

[12] J.-D. Pillet, C. H. L. Quay, P. Morfin, C. Bena, A. L. Yeyati, and P. Joyez, Andreev bound states in supercurrent-carrying carbon nanotubes revealed, Nat. Phys. **6**, 965 (2010).

[13] J. J. Wesdorp, L. Grünhaupt, A. Vaartjes, M. Pita-Vidal, A. Bargerbos, L. J. Splitthoff, P. Krogstrup, B. van Heck, and G. de Lange, Dynamical polarization of the fermion parity in a nanowire Josephson junction, Phys. Rev. Lett. **131**, 117001 (2023).

[14] J. M. van Ruitenbeek, A. Alvarez, I. Piñeyro, C. Grahmann, P. Joyez, M. H. Devoret, D. Esteve, and C. Urbina, Adjustable nanofabricated atomic size contacts, Rev. Sci. Instrum. **67**, 108 (1996).

[15] A. Tagliacozzo and A. L. Yeyati, Mesoscopic features in nanoscale superconducting devices, in *Fundamentals and Frontiers of the Josephson Effect*, edited by F. Tafuri, Springer Series in Materials Science (Springer, Cham, 2019), pp. 147–207.

[16] E. J. H. Lee, X. Jiang, M. Houzet, R. Aguado, C. M. Lieber, and S. De Franceschi, Spin-resolved Andreev levels and parity crossings in hybrid superconductor–semiconductor nanostructures, Nat. Nanotechnol. **9**, 79 (2014).

[17] D. J. van Woerkom, A. Proutski, B. van Heck, D. Bouman, J. I. Väyrynen, L. I. Glazman, P. Krogstrup, J. Nygård, L. P. Kouwenhoven, and A. Geresdi, Microwave spectroscopy of spinful Andreev bound states in ballistic semiconductor Josephson junctions, Nat. Phys. **13**, 876 (2017).

[18] M. Hays, G. de Lange, K. Serniak, D. J. van Woerkom, D. Bouman, P. Krogstrup, J. Nygård, A. Geresdi, and M. H. Devoret, Direct microwave measurement of Andreev-bound-state dynamics in a semiconductor-nanowire Josephson junction, Phys. Rev. Lett. **121**, 047001 (2018).

[19] L. Tosi, C. Metzger, M. F. Goffman, C. Urbina, H. Pothier, S. Park, A. L. Yeyati, J. Nygård, and P. Krogstrup, Spin-orbit splitting of Andreev states revealed by microwave spectroscopy, Phys. Rev. X **9**, 011010 (2019).

[20] M. Hays, V. Fatemi, D. Bouman, J. Cerrillo, S. Diamond, K. Serniak, T. Connolly, P. Krogstrup, J. Nygård, A. Levy Yeyati

et al., Coherent manipulation of an Andreev spin qubit, Science **373**, 430 (2021).

[21] E. Prada, P. San-Jose, M. W. A. de Moor, A. Geresdi, E. J. H. Lee, J. Klinovaja, D. Loss, J. Nygård, R. Aguado, and L. P. Kouwenhoven, From Andreev to Majorana bound states in hybrid superconductor–semiconductor nanowires, Nat. Rev. Phys. **2**, 575 (2020).

[22] F. J. Matute-Cañadas, C. Metzger, S. Park, L. Tosi, P. Krogstrup, J. Nygård, M. F. Goffman, C. Urbina, H. Pothier, and A. L. Yeyati, Signatures of interactions in the Andreev spectrum of nanowire Josephson junctions, Phys. Rev. Lett. **128**, 197702 (2022).

[23] V. Fatemi, P. D. Kurilovich, M. Hays, D. Bouman, T. Connolly, S. Diamond, N. E. Frattini, V. D. Kurilovich, P. Krogstrup, J. Nygård *et al.*, Microwave susceptibility observation of interacting many-body Andreev states, Phys. Rev. Lett. **129**, 227701 (2022).

[24] P. Krogstrup, N. L. B. Ziino, W. Chang, S. M. Albrecht, M. H. Madsen, E. Johnson, J. Nygård, C. M. Marcus, and T. S. Jespersen, Epitaxy of semiconductor–superconductor nanowires, Nat. Mater. **14**, 400 (2015).

[25] J.-D. Pillet, P. Joyez, R. Žitko, and M. F. Goffman, Tunneling spectroscopy of a single quantum dot coupled to a superconductor: From Kondo ridge to Andreev bound states, Phys. Rev. B **88**, 045101 (2013).

[26] A. Martín-Rodero and A. Levy Yeyati, Josephson and Andreev transport through quantum dots, Adv. Phys. **60**, 899 (2011).

[27] A. F. Andreev, Electron spectrum of the intermediate state of superconductors, J. Exptl. Theoret. Phys. (U.S.S.R.) **49**, 655 (1966) [Sov. Phys. JETP **22**, 45 (1966)].

[28] I. O. Kulik, Macroscopic quantization and the proximity effect in S-N-S junctions, Zh. Eksp. Teor. Fiz. **57**, 1745 (1970) [Sov. Phys. JETP **30**, 944 (1970)].

[29] A. Furusaki and M. Tsukada, Current-carrying states in Josephson junctions, Phys. Rev. B **43**, 10164 (1991).

[30] P. W. Anderson and J. M. Rowell, Probable observation of the Josephson superconducting tunneling effect, Phys. Rev. Lett. **10**, 230 (1963).

[31] L. I. Glazman and K. A. Matveev, Resonant Josephson current through Kondo impurities in a tunnel barrier, Pis'ma Zh. Eksp. Teor. Fiz. **49**, 570 (1989) [JETP Lett **49**, 659 (1989)].

[32] M.-S. Choi, M. Lee, K. Kang, and W. Belzig, Kondo effect and Josephson current through a quantum dot between two superconductors, Phys. Rev. B **70**, 020502(R) (2004).

[33] A. Oguri and Y. Tanaka, Quantum phase transition in a minimal model for the Kondo effect in a Josephson junction, J. Phys. Soc. Jpn. **73**, 2494 (2004).

[34] Y. Tanaka, A. Oguri, and A. Hewson, Kondo effect in asymmetric Josephson couplings through a quantum dot, New J. Phys. **9**, 115 (2007).

[35] C. Karrasch, A. Oguri, and V. Meden, Josephson current through a single Anderson impurity coupled to BCS leads, Phys. Rev. B **77**, 024517 (2008).

[36] A. Kadlecová, M. Žonda, V. Pokorny, and T. Novotny, Practical guide to quantum phase transitions in quantum-dot-based tunable Josephson junctions, Phys. Rev. Appl. **11**, 044094 (2019).

[37] V. Meden, The Anderson-Josephson quantum dot—A theory perspective, J. Phys.: Condens. Matter **31**, 163001 (2019).

[38] P. D. Kurilovich, V. D. Kurilovich, V. Fatemi, M. H. Devoret, and L. I. Glazman, Microwave response of an Andreev bound state, Phys. Rev. B **104**, 174517 (2021).

[39] C. Hermansen, A. L. Yeyati, and J. Paaske, Inductive microwave response of Yu-Shiba-Rusinov states, Phys. Rev. B **105**, 054503 (2022).

[40] T. Meng, S. Florens, and P. Simon, Self-consistent description of Andreev bound states in Josephson quantum dot devices, Phys. Rev. B **79**, 224521 (2009).

[41] R. S. Deacon, Y. Tanaka, A. Oiwa, R. Sakano, K. Yoshida, K. Shibata, K. Hirakawa, and S. Tarucha, Tunneling spectroscopy of Andreev energy levels in a quantum dot coupled to a superconductor, Phys. Rev. Lett. **104**, 076805 (2010).

[42] W. Chang, V. E. Manucharyan, T. S. Jespersen, J. Nygård, and C. M. Marcus, Tunneling spectroscopy of quasiparticle bound states in a spinful Josephson junction, Phys. Rev. Lett. **110**, 217005 (2013).

[43] S. Li, N. Kang, P. Caroff, and H. Q. Xu, 0-π phase transition in hybrid superconductor–InSb nanowire quantum dot devices, Phys. Rev. B **95**, 014515 (2017).

[44] E. J. H. Lee, X. Jiang, R. Žitko, R. Aguado, C. M. Lieber, and S. De Franceschi, Scaling of subgap excitations in a superconductor-semiconductor nanowire quantum dot, Phys. Rev. B **95**, 180502(R) (2017).

[45] A. Bargerbos, M. Pita-Vidal, R. Žitko, J. Ávila, L. J. Splitthoff, L. Grünhaupt, J. J. Wesdorp, C. K. Andersen, Y. Liu, L. P. Kouwenhoven *et al.*, Singlet-doublet transitions of a quantum dot Josephson junction detected in a transmon circuit, PRX Quantum **3**, 030311 (2022).

[46] A. Bargerbos, M. Pita-Vidal, R. Žitko, L. J. Splitthoff, L. Grünhaupt, J. J. Wesdorp, Y. Liu, L. P. Kouwenhoven, R. Aguado, C. K. Andersen *et al.*, Spectroscopy of spin-split Andreev levels in a quantum dot with superconducting leads, Phys. Rev. Lett. **131**, 097001 (2023).

[47] See Supplemental Material at http://link.aps.org/supplemental/10.1103/PhysRevB.109.134506 for additional data on device fabrication, measurement setup, single-tone and two-tone measurements, and details of theoretical model, which includes Refs. [56–59].

[48] C. Metzger, S. Park, L. Tosi, C. Janvier, A. A. Reynoso, M. F. Goffman, C. Urbina, A. Levy Yeyati, and H. Pothier, Circuit-QED with phase-biased Josephson weak links, Phys. Rev. Res. **3**, 013036 (2021).

[49] S. Park, C. Metzger, L. Tosi, M. F. Goffman, C. Urbina, H. Pothier, and A. Levy Yeyati, From adiabatic to dispersive readout of quantum circuits, Phys. Rev. Lett. **125**, 077701 (2020).

[50] F. Pedregosa, G. Varoquaux, A. Gramfort, V. Michel, B. Thirion, O. Grisel, M. Blondel, P. Prettenhofer, R. Weiss, V. Dubourg *et al.*, Scikit-learn: Machine learning in Python, J. Mach. Learn. Res. **12**, 2825 (2011).

[51] C. Metzger, Spin & charge effects in Andreev bound states, Ph.D thesis, Université Paris-Saclay, 2022, https://hal.science/tel-03892704.

[52] V. Levajac, H. Barakov, G. P. Mazur, N. van Loo, L. P. Kouwenhoven, Y. V. Nazarov, and J.-Y. Wang, Supercurrent in the presence of direct transmission and a resonant localized state, arXiv:2310.03296.

[53] D. G. Olivares, A. Levy Yeyati, L. Bretheau, Ç. Ö. Girit, H. Pothier, and C. Urbina, Dynamics of quasiparticle trapping in Andreev levels, Phys. Rev. B **89**, 104504 (2014).

[54] N. Ackermann, A. Zazunov, S. Park, R. Egger, and A. L. Yeyati, Dynamical parity selection in superconducting weak links, Phys. Rev. B **107**, 214515 (2023).

[55] M. Pita-Vidal, A. Bargerbos, R. Žitko, L. J. Splitthoff, L. Grünhaupt, J. J. Wesdorp, Y. Liu, L. P. Kouwenhoven, R. Aguado, B. van Heck *et al.*, Direct manipulation of a superconducting spin qubit strongly coupled to a transmon qubit, Nat. Phys. **19**, 1110 (2023).

[56] M. Greenfeld, D. S. Pavlichin, H. Mabuchi, and D. Herschlag, Single molecule analysis research tool (SMART): An integrated approach for analyzing single molecule data, PLoS ONE **7**, e30024 (2012).

[57] S. Gammelmark, K. Mølmer, W. Alt, T. Kampschulte, and D. Meschede, Hidden Markov model of atomic quantum jump dynamics in an optically probed cavity, Phys. Rev. A **89**, 043839 (2014).

[58] I. Affleck, J.-S. Caux, and A. M. Zagoskin, Andreev scattering and Josephson current in a one-dimensional electron liquid, Phys. Rev. B **62**, 1433 (2000).

[59] J. J. Wesdorp, F. J. Matute-Cañadas, A. Vaartjes, L. Grünhaupt, T. Laeven, S. Roelofs, L. J. Splitthoff, M. Pita-Vidal, A. Bargerbos, D. J. van Woerkom *et al.*, Microwave spectroscopy of interacting Andreev spins, Phys. Rev. B **109**, 045302 (2024).